crystals

MDPI

Article

Effects of Co- and Ni-Based Brazing Filler Alloys on the Microstructure and Tensile Properties of DD5 Single-Crystal Superalloy

Dongling Yang [1,2], Shusuo Li [1,*], Taili Chen [2,*], Geng Li [1], Bin Hu [3], Tinghong Hou [2], Xuan Zhao [2] and Kuilin Luo [2]

[1] Research Institute of Aero-Engine, Beihang University, Beijing 100191, China
[2] Cheng Du Hang Li (Group) Industrial Co, Ltd., Chengdu 610093, China
[3] School of Materials Science and Engineering, Beihang University, Beijing 100191, China
* Correspondence: lishs@buaa.edu.cn (S.L.); tlchen665@foxmail.com (T.C.)

Abstract

DD5 Ni-based single-crystal superalloy was diffusion-brazed using Ni-based (NB) and Co-based (CB) filler alloys to systematically investigate the effects of filler alloy composition on joint microstructure, secondary phase formation, microhardness, and high-temperature tensile properties at 870 °C. The relationship between microstructural characteristics and fracture behavior was also examined. Both filler alloys produced sound metallurgical joints without obvious pores or cracks. The CB joint exhibited a brazed seam width of approximately 353.1 μm, slightly larger than that of the NB joint (348.0 μm), while significant differences were observed in grain size and secondary phase distribution. The CB joint exhibited a finer polycrystalline microstructure, with an average grain size of 56.3 μm, compared with 79.5 μm for the NB joint. Microstructural characterization revealed that the CB joint consisted primarily of a NiCo-rich γ matrix and skeletal WCo-rich and WCr-rich secondary phases, with area fractions of approximately 3.1% and 0.2%, respectively. In contrast, the NB joint contained WCr-rich and Cr-rich σ phases, with corresponding area fractions of 1.6% and 0.9%. The CB joint exhibited a higher peak microhardness of approximately 690 HV0.2 compared with 610 HV0.2 for the NB joint, which may be associated with the strengthening contribution of the WCo-rich phase. At 870 °C, the CB joint achieved an average tensile strength of 630 MPa, representing an improvement of approximately 34% over the NB joint (470 MPa). Fractographic analysis revealed that the CB joint exhibited a mixed fracture mode characterized by dimples and localized cleavage-like steps, whereas the NB joint displayed predominantly cleavage-like fracture features, with cracks preferentially initiating and propagating near the WCr-rich and Cr-rich σ phases. In comparison, the WCo-rich phase in the CB joint may contribute to enhanced local deformation resistance and reduced susceptibility to rapid crack propagation. These findings indicate that the nature, morphology, and spatial distribution of secondary phases play important roles in governing the high-temperature tensile behavior of brazed joints, highlighting the potential of Co-based filler alloys for improving the high-temperature load-bearing capability of DD5 single-crystal superalloy joints.

Keywords: single-crystal super-alloy; diffusion brazing; microstructure; mechanical properties

Academic Editor: Umberto Prisco

Received: 1 October 2026
Revised: 5 November 2026
Accepted: 16 November 2026
Published: 18 November 2026

Copyright: © 2026 by the authors. Licensee MDPI, Basel, Switzerland. This article is an open access article distributed under the terms and conditions of the Creative Commons Attribution (CC BY) license.

1. Introduction

Ni-based single-crystal superalloys are widely employed in high-pressure turbine blades of aero-engines owing to their outstanding high-temperature performance [1–4]. However, prolonged thermomechanical service can lead to irreversible damage in turbine blades, particularly thermomechanical fatigue cracks, thereby degrading blade performance and threatening the safe and reliable operation of the engine [5–9]. Given the high manufacturing cost and complex fabrication processes associated with single-crystal turbine blades, developing reliable repair techniques capable of restoring both geometric integrity and long-term high-temperature service performance is of great significance [10]. Brazing is particularly well suited for repairing narrow cracks and localized damage in turbine components, as it enables effective metallurgical joining without melting the base material [11,12].

The addition of melting-point depressants such as B and Si promotes the formation of a liquid phase and improves the wettability and gap-filling capability of the filler alloy. These elements diffuse into the base material, raising the local solidus temperature of the joint and facilitating isothermal solidification of the liquid phase [13]. During cooling, the residual liquid, enriched with slow-diffusing solutes such as B, Si, Cr, and W, solidifies to form a non-isothermally solidified zone, which typically contains eutectic structures, borides, carbides, and other hard and brittle phases [14–16]. Furthermore, outward diffusion of B into the base metal induces the precipitation of M_3B_2-and M_5B_3-type borides within the diffusion-affected zone [15]. The morphology, size, and distribution of these secondary phases significantly influence the local hardness and deformation behavior of the brazed joint.

To improve the performance of brazed joints in single-crystal superalloys, extensive research has been conducted on filler metal composition design and process optimization [17]. Ni-based filler metals exhibit good chemical compatibility with Ni-based single-crystal substrates and are therefore widely employed. The joining behavior of a Ni-Cr-Co-W-Mo-B interlayer was investigated [18], while the effects of brazing temperature and holding time on the microstructural evolution of DD5 joints brazed with BNi-2 filler metal were systematically investigated [19]. In addition to experimental characterisation, first-principles calculations may provide insights into the changes in the composition of the brazing process in heterogeneous materials, in terms of local structure and electronic effects [20].

In addition, Ni-Cr-Ta and high-entropy alloy fillers have also been explored to enhance the joint strength of single-crystal superalloys [12,21]. The introduction of mixed powder and rapid epitaxial brazing methods has been shown to effectively reduce the content of melting-point depressants, accelerate isothermal solidification, and improve gap-filling capability [22]. However, the formation of brittle phases in Ni-based brazed joints remains an inherent challenge. Co-based filler alloys offer an alternative potential solution for repairing Ni-based single-crystal superalloys. Owing to their higher Cr and Co contents, such fillers may influence solute partitioning, secondary phase precipitation, interfacial morphology, and oxidation-assisted damage behavior during high-temperature exposure. Previous studies have demonstrated that the use of Co-based interlayers can yield relatively sound joints in single-crystal superalloys, with the mechanical properties of the brazed joints being substantially improved [11,23].

However, direct comparative studies on the microstructure and mechanical properties of Ni-based and Co-based brazed joints under similar gap sizes and base material conditions remain scarce. To address this issue, DD5 single-crystal superalloy was brazed using Ni-based and Co-based filler alloys, followed by a comparative investigation of the microstructural characteristics and interfacial morphologies of the resulting joints. In ad-

dition, the microhardness and the tensile properties of the two joints at 870 °C were systematically evaluated, enabling a direct quantitative comparison of the mechanical performance between the two joining systems.

2. Experimental Materials and Methods

Considering its wide application in aero-engine turbine blades [19,24], DD5 single-crystal superalloy was selected as the substrate material in this study. The standard heat treatment consisted of holding at 1300 °C for 4 h, and the nominal chemical composition is given in Table 1. After the heat treatment, the microstructure is shown in Figure 1a, which reveals a fully solutionized γ/γ′ two-phase structure with well-cuboidal γ′ precipitates; the average size of the γ′ phase is approximately 863 nm. Two types of filler metals were employed for brazing: a Ni-based braze superalloy (NB) and a Co-based braze superalloy (CB). Their actual chemical compositions were determined by inductively coupled plasma optical emission spectrometry (ICP-OES), and the results are listed in Table 2.

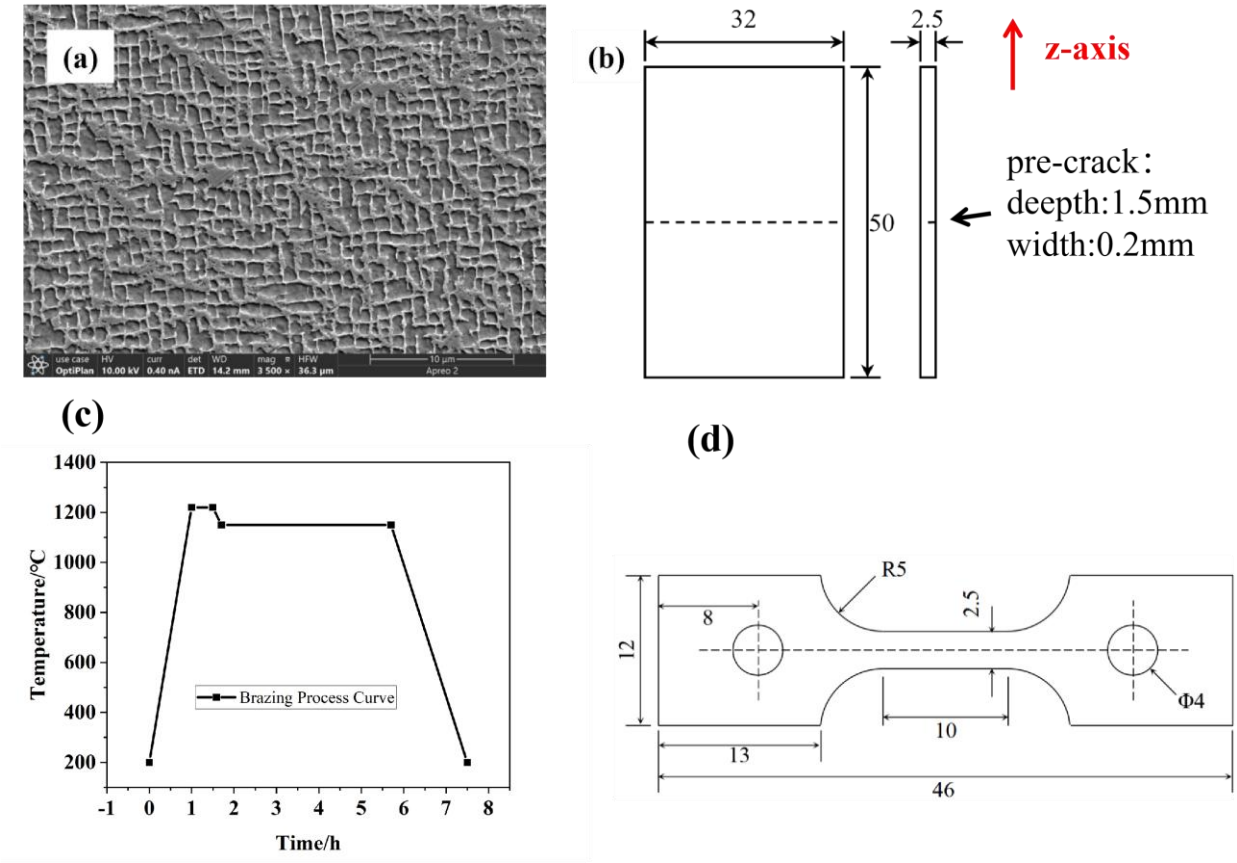


Figure 1. (**a**) Microstructure of DD5 after standard heat treatment; (**b**) three-dimensional dimensions of the brazed specimen; (**c**) brazing process curve; and (**d**) dimensions of the tensile specimen.

Table 1. Nominal chemical composition of single-crystal superalloy.

Element	C	Cr	Co	W	Mo	Ta
wt.%	0.045	7.0	8.0	5.0	2.0	7.0
Element	**Al**	**Hf**	**B**	**Re**	**Ni**	
wt.%	6.2	0.2	0.004	3.0	Bal.	

Table 2. Composition of the braze alloys (wt.%).

No.	Al	B	C	Cr	W	Ni	Co
NB	2.0	3.0	0.01	9.0	4.0	Bal.	10.0
CB	0	2.0	0.02	21.0	11.0	20.0	Bal.

To simulate the geometric characteristics of service cracks in turbine guide vanes, a narrow slit 0.2 mm wide and 1.5 mm deep was machined in the specimen along the direction perpendicular to the *Z*-axis; its dimensions are schematically shown in Figure 1b. Before brazing, all specimens were subjected to fluoride ion cleaning to remove surface oxides, oil stains, and other impurities. The two brazing filler alloy powders were each mechanically mixed with the same DD5 alloy powder at a mass ratio of 3:7, and a suitable amount of organic binder was added to prepare a paste for diffusion brazing. Using Pandat 2021 thermodynamic calculation software together with the Pan_Ni V2021 and Pan_Co V2021 databases, the liquidus temperatures of the Ni-based (NB) and Co-based (CB) filler alloys were calculated to be approximately 1180 °C and 1203 °C, respectively. After the paste was applied, the specimens were vacuum brazed according to the process curve shown in Figure 1c: the NB and CB specimens were held at 1220 °C for 0.5 h, and then both were held at 1150 °C for 4 h. After furnace cooling to 200 °C, they were removed.

The low-magnification morphology of the brazing seam region was observed using a Zeiss Axio Observer 7m optical microscope (Carl Zeiss Microscopy GmbH, Oberkochen, Germany). The microstructure of the brazing seam and the fracture morphology of the high-temperature tensile specimens were examined using a Thermo Fisher Apreo 2S scanning electron microscope (SEM) (Thermo Fisher Scientific, Waltham, MA, USA)., coupled with a Bruker XFlash 6-60 energy dispersive spectrometer (EDS) (Bruker Nano GmbH, Berlin, Germany)., for point composition analysis and elemental mapping. Meanwhile, the precipitates in the brazing seam were characterized by F20 transmission electron microscopy (TEM). (FEI Company, Eindhoven, The Netherlands). High-temperature tensile specimens with dimensions of 46 mm × 12 mm, as shown in Figure 1d, were tested using an ETM305D-T5 electronic universal testing machine (Shenzhen WANCE Testing Machine Co., Ltd., Shenzhen, China), at 870 °C. The tests were conducted under crosshead displacement control, with a crosshead speed of 0.4 mm/min before yielding and 2 mm/min after yielding. Three specimens were tested for each brazing condition.

3. Results and Discussion

3.1. Microstructure of Brazed Joint

Microstructural characterization was carried out to assess the overall morphology and defect distribution of the brazed joints. The optical morphologies of the NB and CB brazed joints were examined, and the corresponding microstructural features are presented in Figure 2a,b. Both brazed joints were free of obvious pores and cracks, and well-defined diffusion zones were observed in the two specimens, demonstrating good metallurgical bonding and effective gap-filling capability at a joint gap of 0.2 mm. The total widths of the CB brazed joints and NB brazed joints were 353.1 μm and 348.0 μm, respectively.

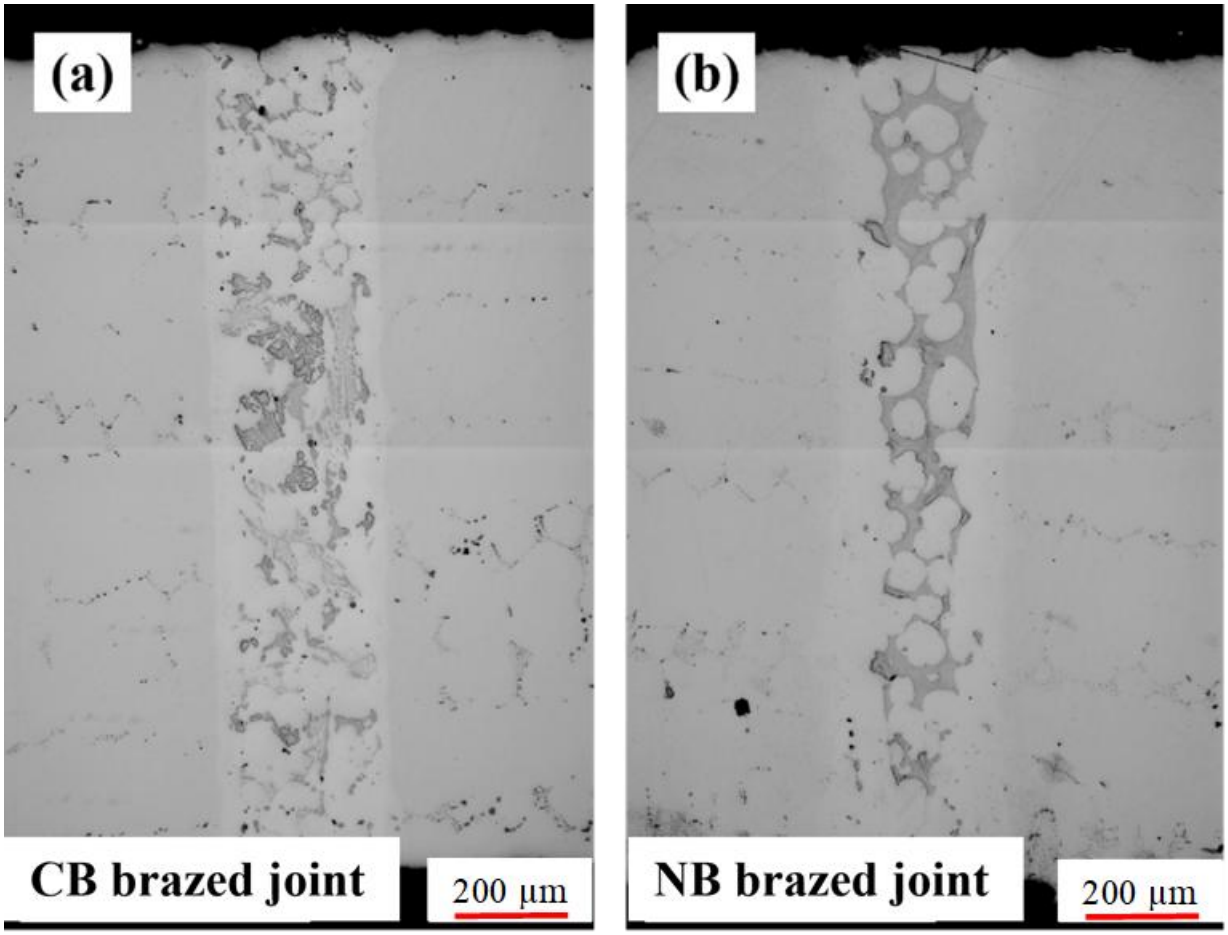


Figure 2. Optical microstructure of the CB and NB brazed joint specimens: (**a**) CB brazed joint; (**b**) NB brazed joint.

The detailed microstructural evolution of the brazed joints was investigated using SEM and EDS, with a particular focus on the morphological discrepancies between the Ni-based (NB) and Co-based (CB) specimens. As illustrated in Figure 3, NB brazed joint exhibit a typical three-layer structure comprising the Base Material Zone (BMZ), Isothermal Solidification Zone (ISZ), and Non-Isothermal Solidification Zone (NSZ).

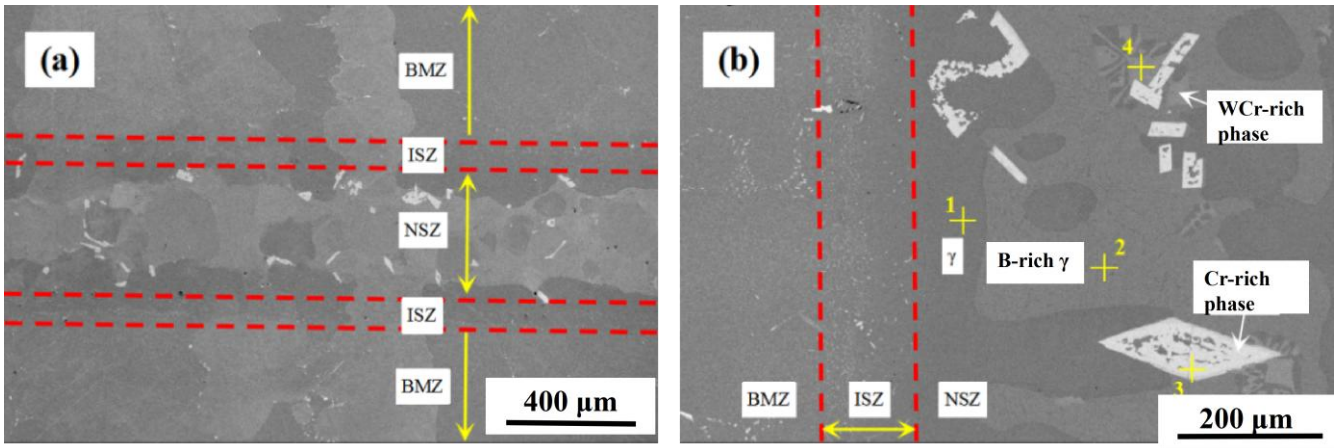


Figure 3. Microstructure of the NB brazed joint of the SEM: (**a**) low-magnification; (**b**) high-magnification.

As shown in Figure 3, the Ni-based brazed joint exhibits pronounced microstructural and compositional heterogeneity across the brazed region. The joint can be divided into

the base material zone (BMZ), isothermal solidification zone (ISZ), and non-isothermal solidification zone (NSZ). In the enlarged BSE image, several constituents with distinctly different contrasts and morphologies are observed within the brazed region, including a relatively uniform matrix and coarse blocky or irregular secondary phases. The EDS results in Table 3 reveal significant elemental partitioning among these regions. Region 1 is primarily enriched in Ni (57.7 at.%) and contains no detectable B, indicating a Ni-rich γ matrix constituent. Region 2 also remains Ni-rich (53.7 at.%) but contains 11.0 at.% B, suggesting appreciable local enrichment of the melting-point depressant within the matrix. In contrast, region 3 exhibits pronounced Cr and B enrichment, with Cr and B contents of 48.77 at.% and 8.98 at.%, respectively, while the Ni content decreases significantly to 12.79 at.%, suggesting the formation of a Cr-rich secondary phase. Region 4, however, is characterized by substantial enrichment of both Cr (29.19 at.%) and W (19.04 at.%), accompanied by a relatively low Ni content (17.90 at.%) and a B content of 5.23 at.%, indicating the formation of a WCr-rich secondary phase. These compositional differences suggest preferential partitioning of Cr, W, and B into distinct secondary phases during the solidification of the NB brazed joint.

Table 3. Composition of the phases in NB brazed joint (at.%).

Region	Al	B	C	Co	Cr	Mo	Re	Ta	W	Ni
1	6.6	/	21.2	6.8	6.6	/	/	/	1.1	57.7
2	2.4	11.0	19.5	6.5	5.7	/	/	0.7	0.5	53.7
3	/	8.98	17.81	4.96	48.77	1.4	/	/	5.29	12.79
4	/	5.23	22.11	5.89	29.19	/	/	/	19.04	17.90

Moreover, the differences in Ni, Cr, B, W, and other alloying elements between these two Cr-rich constituents suggest that the secondary-phase region is itself chemically heterogeneous. Overall, the results indicate that substantial redistribution of Ni, W and Cr occurs during solidification of the Ni-based brazed joint, leading to the formation of coarse Cr-rich secondary phases within the NSZ and consequently increasing the chemical and microstructural heterogeneity of the brazed seam. The B and C contents obtained by EDS are considered semi-quantitative and are mainly used to evaluate relative elemental partitioning.

Figure 4 presents the TEM-EDS elemental mapping results obtained from a representative region. Pronounced elemental partitioning can be observed among the different microstructural regions. In particular, Cr is strongly enriched in the second-phase region, whereas Ni and W exhibit varying degrees of depletion in the corresponding area, indicating a clear inverse partitioning behavior between Cr and Ni/W. In contrast, Co and Mo show relatively weak spatial variations, and no apparent enrichment of Al is observed within the Cr-rich region. In addition, under the present EDS mapping conditions, the distribution of C does not exhibit an obvious spatial correlation with the Cr-enriched area. These results indicate that the second phase is primarily characterized by Cr enrichment accompanied by Ni and W depletion, suggesting that its formation involves pronounced local redistribution of alloying elements.

https://doi.org/10.3390/cryst16110728

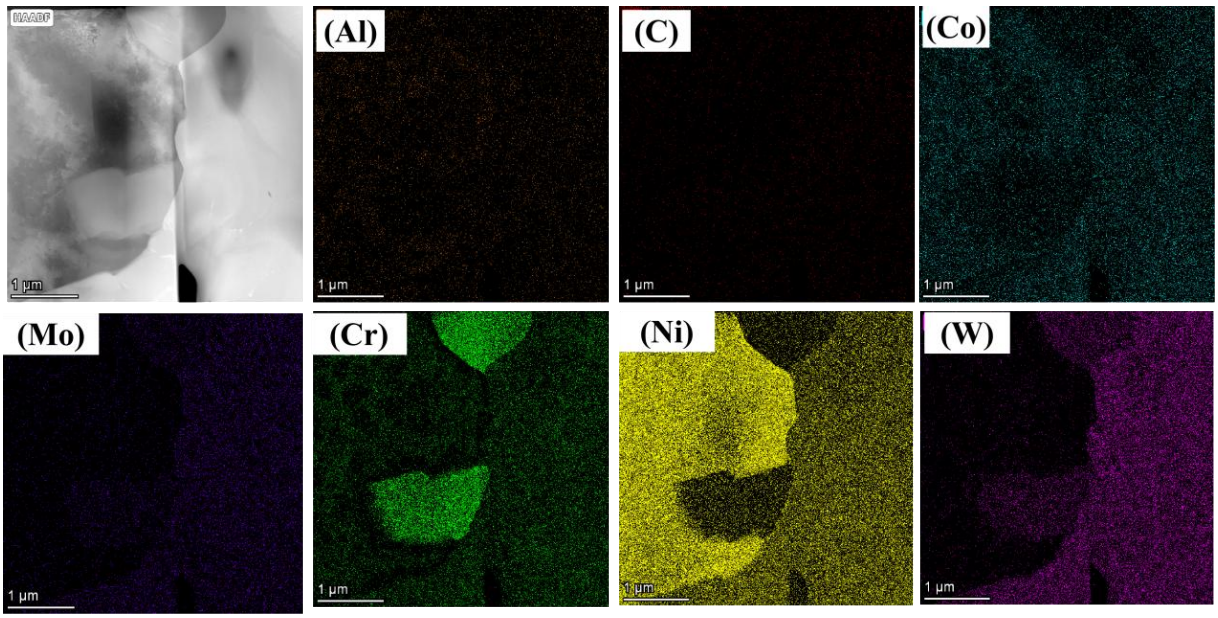


Figure 4. HAADF images and element distribution of Ni-based brazed joints.

As shown in Figure 5, TEM characterization was performed on the precipitate formed within the brazing region. The selected-area electron diffraction (SAED) pattern exhibits a well-defined periodic array of diffraction spots and can be indexed to the tetragonal σ-type phase, with the zone axis identified as $[010]_\sigma$. The major reflections can be assigned to the $(400)_\sigma$, $(20\text{-}2)_\sigma$ planes, together with their higher-order reflections, and the geometrical relationships among these spots are in good agreement with the crystallographic characteristics of the σ phase. In addition, TEM-EDS elemental mapping reveals pronounced Cr enrichment in the precipitate, accompanied by depletion of Ni and W, whereas the spatial variations of Co and Mo are relatively weak. No obvious Al enrichment is observed in the Cr-rich region, and no clear spatial correlation is detected between C and the precipitate. Based on the combined diffraction analysis and compositional characteristics, the brazing joint precipitate can be identified as a Cr-rich σ phase. Its formation indicates significant local elemental redistribution during brazing joint solidification, with Cr segregation providing favorable conditions for the precipitation of the σ phase.

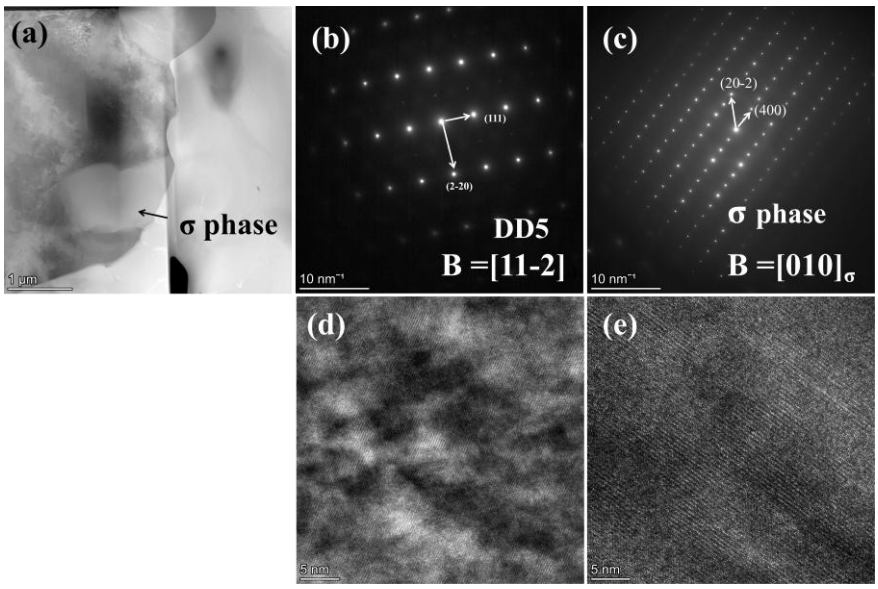


Figure 5. (**a**) TEM morphologies of brazing joint; (**b**) DD5 diffraction spots B = [11-2]; (**c**) diffraction spots B = [010]; (**d**) high-resolution images of DD5; and (**e**) high-resolution images of Cr-rich phase.

https://doi.org/10.3390/cryst16110728

As shown in Figure 6, the Co-based brazed joint exhibits a heterogeneous but relatively continuous microstructure across the brazed region. The joint consists of the base material region, a relatively uniform interfacial region, and a central non-isothermally solidified region characterized by a pronounced skeletal morphology. The chemical compositions of the different regions in the CB brazed joint are summarized in Table 4. Regions 1 and 2 are primarily composed of Ni and Co, with Ni contents of 40.5 at.% and 50.1 at.% and Co contents of 27.5 at.% and 24.5 at.%, respectively, indicating the formation of a Ni–Co-rich γ matrix. In contrast, region 3 exhibits pronounced enrichment of W (16.5 at.%) and Co (49.1 at.%), accompanied by a substantial reduction in Ni content to 9.1 at.% and an elevated B content of 11.3 at.%, suggesting the formation of a WCo-rich secondary phase. Region 4 is characterized by significant Cr enrichment, with a Cr content reaching 66.45 at.%, while the Ni and Co contents are relatively low at 4.87 at.% and 14.25 at.%, respectively, indicating the formation of a CoCr-rich secondary phase. These compositional differences reveal pronounced elemental partitioning within the CB brazed joint, with Ni and Co predominantly constituting the γ matrix, whereas W and Cr preferentially segregate into distinct secondary phases during solidification.

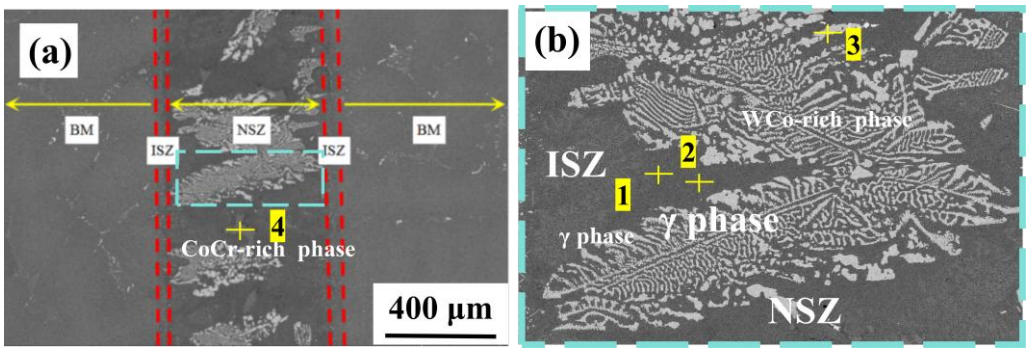


Figure 6. Microstructure of the CB brazed joint and the phases within. (**a**) Microstructure at 400 μm; (**b**) Magnified view of the selected region in (**a**).

Table 4. Composition of the phases in CB brazed joint.

Region	Al	B	C	Co	Cr	Ta	W	Ni
1	3.5	/	15.2	27.5	12.1	0.3	0.9	40.5
2	0.3	2.1	13.8	24.5	7.4	1.8	/	50.1
3	/	11.3	5.0	49.1	7.0	2.8	16.5	9.1
4	/	/	9.83	14.25	66.45	/	4.6	4.87

As shown in Figure 7, the HAADF image of the interface between the DD5 single-crystal superalloy and the brazing region, together with the corresponding TEM-EDS elemental maps, reveals pronounced elemental redistribution across the joint. Co exhibits a relatively higher concentration within the brazing region, whereas Ni and W are enriched on the DD5 substrate side, reflecting both the intrinsic compositional difference between the filler metal and the substrate and the interdiffusion that occurred during joining. Cr shows a certain degree of local enrichment and compositional fluctuation within the brazing joint and near the interface, which may provide favorable compositional conditions for the subsequent formation of Cr-rich precipitates. In contrast, Al and Mo display relatively gradual variations across the interface without obvious localized segregation. The C signal is generally weak, and no clear spatial correlation is observed between C enrichment and either the interface or specific precipitated regions.

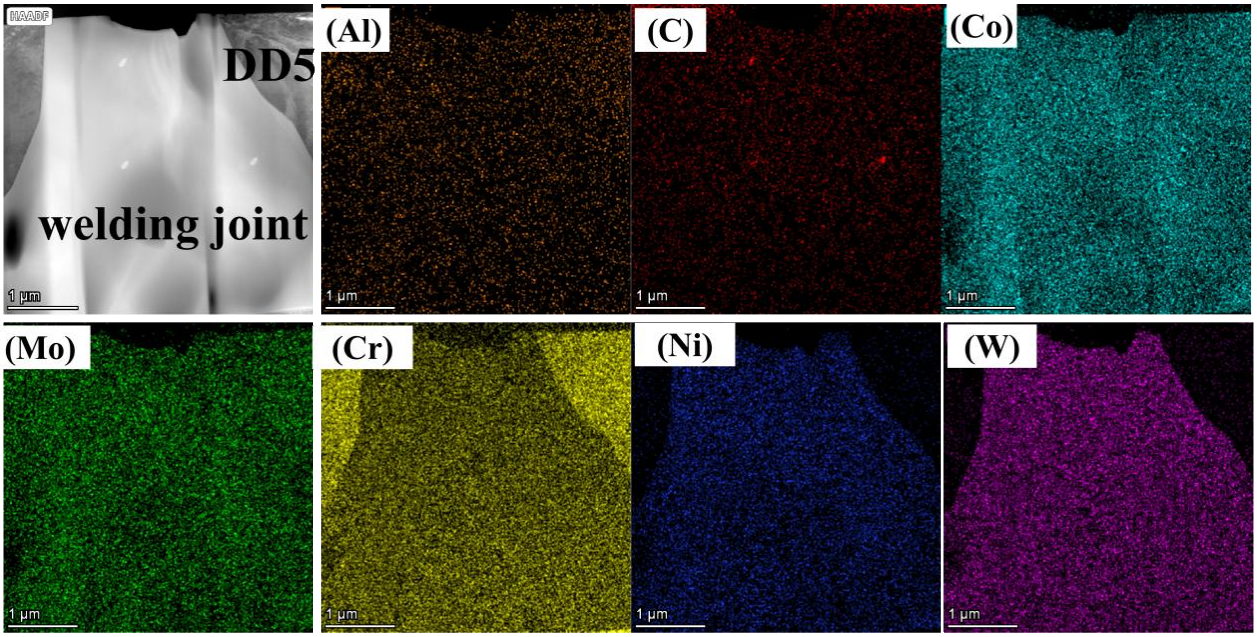


Figure 7. TEM of Co-based brazed joints.

The overall morphology of the Co-based brazing joint is shown in Figure 8a. It can be seen that the brazing joint interface is generally straight and continuous, with no obvious defects such as pores or cracks observed, indicating that the brazing joint has good formation quality. Figure 8b shows the selected-area electron diffraction pattern of the DD5 alloy region, revealing typical ordered superlattice reflections, which indicate that this region exhibits the characteristic $L1_2$ ordered structure. Figure 8c shows the diffraction pattern of the brazing region obtained along the B = [110] crystal zone axis; its main diffraction spots can be identified as characteristic of an FCC structure. It can thus be seen that the main matrix phase of the Co-based brazed joint has an FCC crystal structure, which exhibits good crystal structure compatibility with the FCC structure of the DD5 alloy's γ matrix. This facilitates the formation of a stable metallurgical bond interface between the brazing and the matrix.

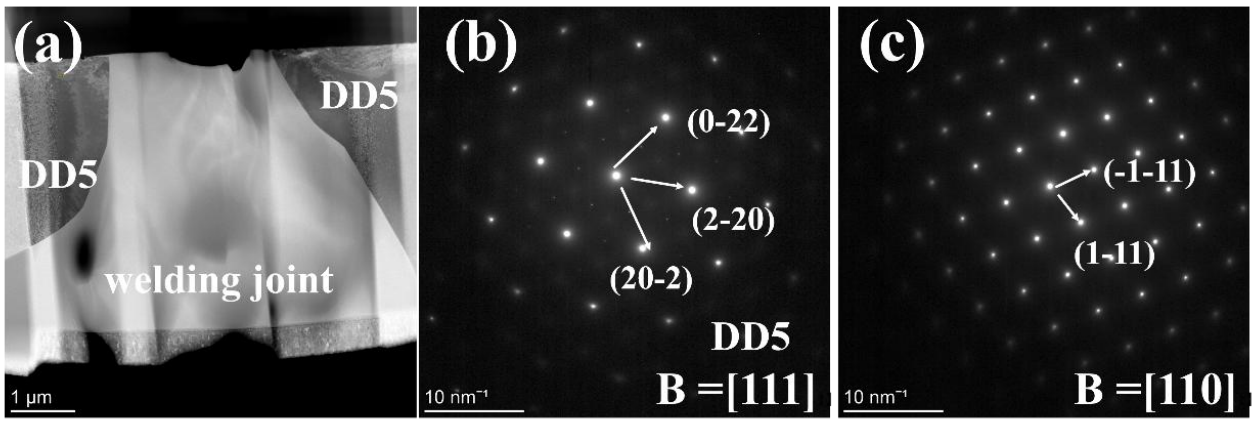


Figure 8. (**a**) TEM of DD5 and Co-based brazed joints. (**b**) DD5 diffraction spot. (**c**) Diffraction spots in the Co-based brazed joints.

Figure 9 presents the EBSD characterization results of the Ni-based and Co-based brazed joints. In both joints, the brazed regions consist of multiple grains with distinct crystallographic orientations, as evidenced by the pronounced orientation variations

within the seams. This indicates that the original single-crystal orientation of the DD5 substrate is not continuously retained across the brazed region, resulting in the formation of a polycrystalline microstructure. However, significant differences in the width and grain morphology of the polycrystalline regions are observed between the two joints.

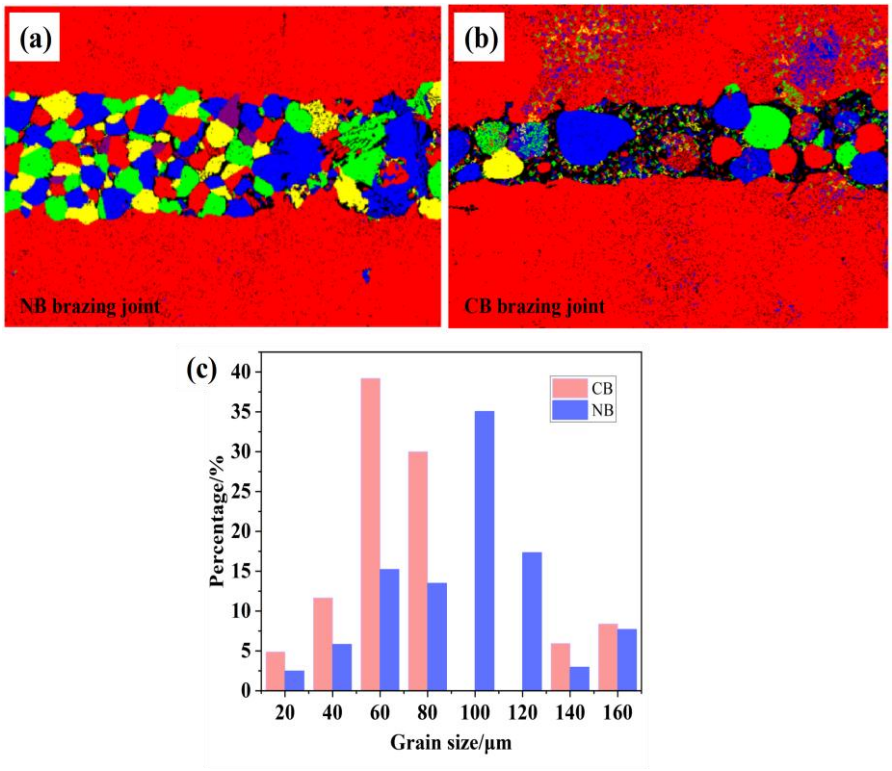


Figure 9. EBSD results of the two brazed joints: (**a**) EBSD result of NB brazing joint; (**b**) EBSD result of CB brazing joint; (**c**) Statistics of grain size of welds for NB joints and CB joints.

Although the overall width of the NB brazed joint (348.0 μm) is slightly smaller than that of the CB brazed joint (353.1 μm), the NB joint exhibits a relatively broader polycrystalline zone containing numerous grains with diverse crystallographic orientations. In contrast, the CB joint displays a noticeably narrower polycrystalline zone. Quantitative EBSD analysis reveals that the CB joint contains approximately 234 grains with an average grain size of 56.3 μm, whereas the NB joint comprises approximately 316 grains with an average grain size of 79.5 μm. These results indicate that the CB joint exhibits a finer-grained microstructure despite containing fewer grains, highlighting the distinct grain size distributions and spatial characteristics of the polycrystalline regions in the two joints.

3.2. High-Temperature Tensile Behavior and Fracture Characteristics at 870 °C

The tensile strength of brazed joints is one of the key mechanical properties for evaluating their service reliability and structural integrity [24,25]. To compare the high-temperature mechanical performance of the two brazed joints, tensile tests were conducted on the NB and CB joints at 870 °C, as shown in Figure 10. The NB joint exhibited an average tensile strength of 470 ± 13 MPa, whereas that of the CB joint reached 630 ± 17 MPa, representing an increase of approximately 34% compared with the NB joint. These results indicate that the CB joint possesses superior tensile strength and load-bearing capability at 870 °C, demonstrating enhanced high-temperature mechanical performance.

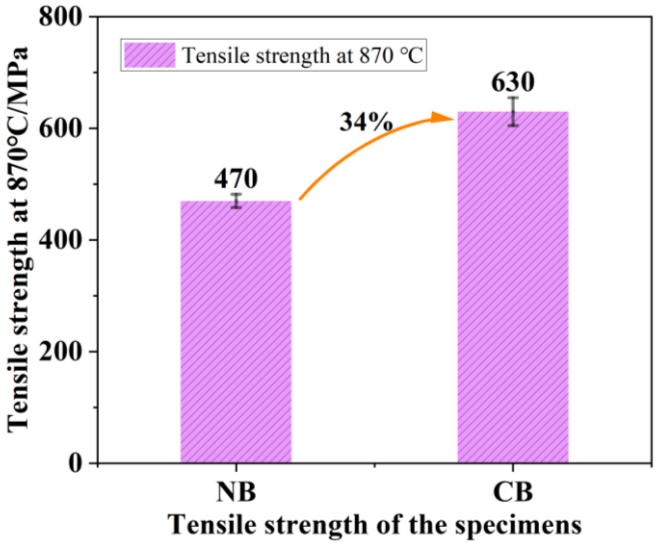


Figure 10. Tensile strength of the specimens.

To elucidate the effects of different brazing filler metals on the high-temperature tensile properties and fracture behavior of the brazed joints, Figure 11 presents the fracture morphologies of the CB and NB joints tested at 870 °C. Distinct differences in fracture characteristics can be observed between the two joints. As shown in Figure 11a,b, the fracture surface of the CB joint is characterized by numerous dimples, indicating considerable plastic deformation accompanied by microvoid nucleation, growth, and coalescence. Further examination reveals that some larger dimples contain localized cleavage-like steps, suggesting a mixed fracture mode dominated by ductile fracture with localized quasi-cleavage features. Similar fracture characteristics have also been reported for joints brazed with Co-based filler metals [26].

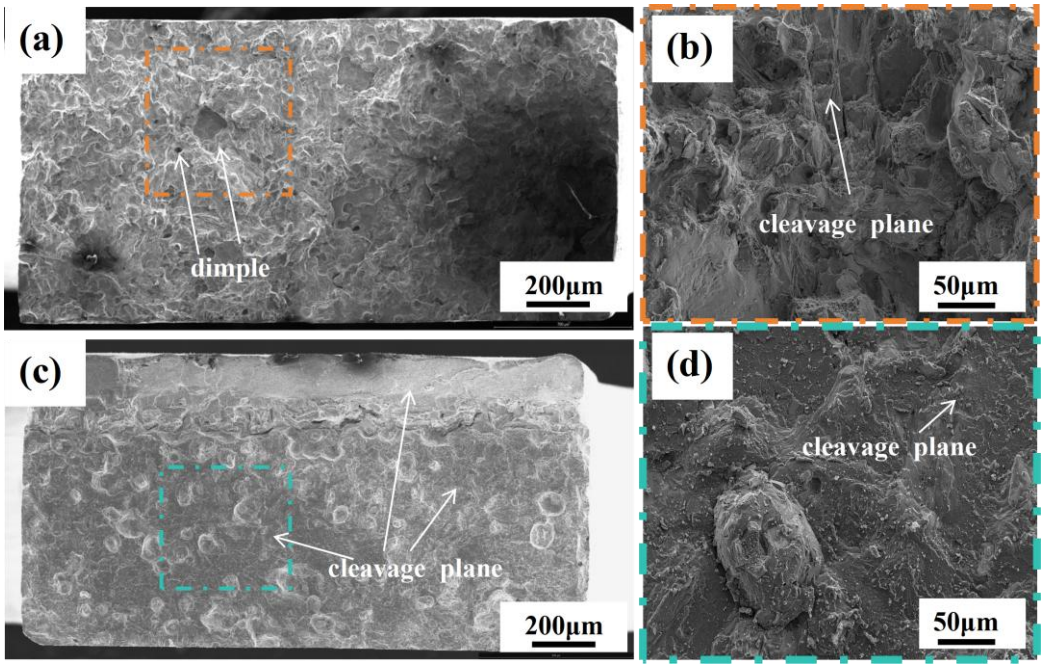


Figure 11. Tensile fracture morphologies of the specimens tested at 870 °C: (**a**,**b**) CB specimens; (**c**,**d**) NB specimens.

According to the EDS results presented in Table 3, the dimpled regions (Points 1 and 2) are primarily associated with the γ phase, whereas the localized cleavage-like features

(Point 3) may be related to the WCo-rich phase. During high-temperature tensile deformation, the γ matrix can accommodate local plastic deformation and dissipate fracture energy, while the dispersed secondary phases may impede dislocation motion and local plastic flow, thereby contributing to an increased resistance to deformation. Furthermore, the interactions between the secondary phases and the surrounding matrix may alter local crack propagation paths and retard continuous crack growth. Therefore, the plastic deformation capability of the γ matrix, together with the potential strengthening and crack-deflection effects of the secondary phases, may contribute to the relatively high tensile strength of the CB joint at elevated temperatures.

In contrast, the NB joint exhibits a distinctly different fracture mode. As shown in Figure 11c, its fracture surface is relatively flat and predominantly characterized by extensive cleavage-like facets and localized steps, indicating a pronounced tendency toward brittle fracture. This fracture morphology is similar to that reported for joints brazed with Ni–Cr–Ta-based filler metals, suggesting that cracks may preferentially propagate along specific crystallographic planes or locally weakened regions [21]. Notably, the fracture surface of the NB joint is not completely smooth but contains numerous localized protrusions and irregular features. Combined with the EDS results of Points 3 and 4 in Table 3, these morphological characteristics may be associated with the presence of WCr-rich and σ phase secondary phases within the brazed seam. During high-temperature tensile loading, the deformation incompatibility between these secondary phases and the surrounding γ matrix may induce localized stress concentrations near the phase boundaries, thereby promoting microcrack initiation. With increasing applied load, these microcracks may propagate through the secondary phases or along their interfaces with the matrix and subsequently coalesce into larger cracks, eventually leading to joint failure. Previous studies have demonstrated that certain brittle precipitates are susceptible to cracking or interfacial decohesion under external loading [27]. Compared with ductile fracture dominated by microvoid coalescence, such crack propagation processes generally involve less plastic deformation and fracture energy dissipation, potentially resulting in premature failure. Consequently, the localized stress concentrations associated with the W- and Cr-rich secondary phases, together with their potential role in promoting crack initiation and propagation, may be responsible for the relatively low high-temperature tensile strength and predominantly brittle fracture behavior of the NB joint.

Figure 12a and b present the longitudinal cross-sectional fracture morphologies of the CB and NB brazed joints, respectively. Distinct differences in crack propagation paths and final fracture locations can be observed between the two joints. Fracture in the CB joint occurs primarily near the isothermal solidification zone (ISZ), whereas the NB joint predominantly fails within the non-isothermal solidification zone. Further examination reveals that cracks in the NB joint preferentially initiate and propagate along the white WCr-rich phase and the gray Cr-rich σ phase, suggesting that these secondary phases may provide preferential pathways for crack initiation and propagation. These observations indicate that the mechanically vulnerable regions differ between the two joints. Specifically, the ISZ and its adjacent regions appear to be the preferential fracture locations in the CB joint, while fracture in the NB joint is more strongly associated with the distribution of secondary phases and local microstructural heterogeneity within the non-isothermal solidification zone.

https://doi.org/10.3390/cryst16110728

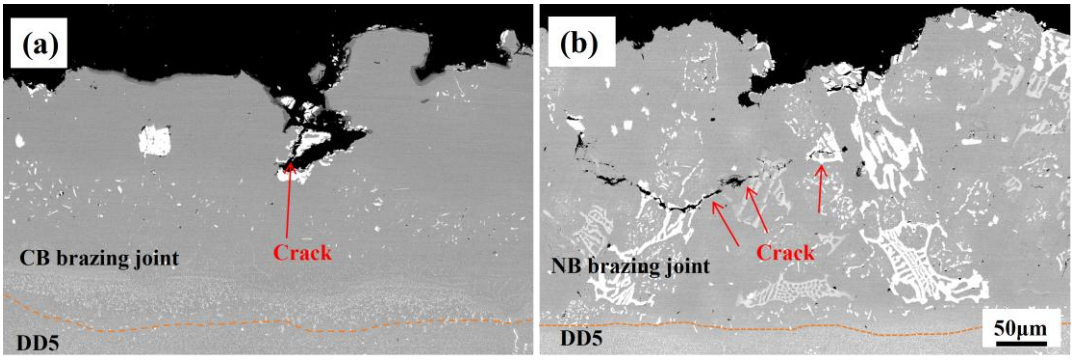


Figure 12. Cross-sectional fracture characteristics of the tensile fracture surface at 870 °C: (**a**) CB specimens; (**b**) NB specimens.

To further investigate the differences in local mechanical properties, microhardness measurements were performed across both brazed joints, as shown in Figure 13. Both joints exhibit localized hardening within the brazed regions, although their hardness distributions differ considerably. The CB joint exhibits a relatively concentrated high-hardness region near the center of the brazed seam, with peak hardness values ranging from approximately 690 HV0.2, indicating a relatively high resistance to localized plastic deformation. In contrast, the NB joint displays a more heterogeneous hardness distribution, characterized by the coexistence of locally hardened and relatively low-hardness regions near the brazed seam. Its peak hardness ranges from approximately 610 HV0.2, reflecting greater microstructural and mechanical heterogeneity within the joint.

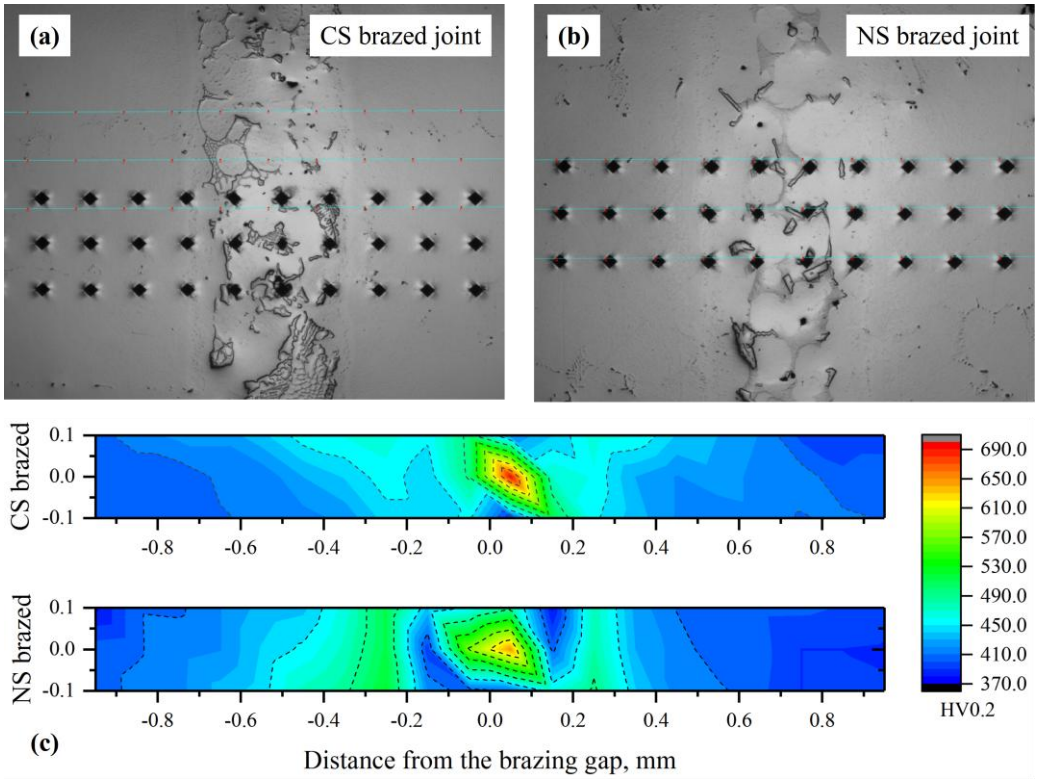


Figure 13. Microhardness characterization of the brazed joints: (**a**) hardness measurement of the CB joint; (**b**) hardness measurement of the NB joint; and (**c**) microhardness distribution maps of the CB and NB joints.

Notably, despite its higher local microhardness, the CB joint achieves a tensile strength of approximately 630 MPa at 870 °C, substantially exceeding that of the NB joint

(approximately 470 MPa). This indicates that the pronounced local hardening in the CB joint does not necessarily result in brittle failure. As revealed by the fracture morphologies in Figure 11, the CB joint exhibits numerous dimples, with smaller secondary dimples occasionally observed within larger ones, suggesting a fracture process dominated by microvoid nucleation, growth, and coalescence. These observations indicate that the secondary phases within the CB seam may enhance the local resistance to plastic deformation without forming continuous brittle crack propagation pathways. Meanwhile, the surrounding γ matrix can accommodate local plastic deformation and redistribute stresses, thereby contributing to the relatively high load-bearing capacity of the CB joint at elevated temperatures.

Further quantitative analysis of the secondary phases reveals that the area fractions of the WCo-rich and CoCr-rich phases in the CB joint are approximately 3.1% and 0.2%, respectively. In comparison, the NB joint contains approximately 1.6% WCr-rich phase and 0.9% σ phase. Although the total area fraction of secondary phases in the CB joint (approximately 3.3%) is higher than that in the NB joint (approximately 2.5%), the CB joint exhibits both higher local microhardness and superior high-temperature tensile strength. This suggests that the mechanical response of the brazed joints is governed not only by the amount of secondary phases but also by their intrinsic mechanical properties, morphology, and spatial distribution. In the CB joint, the relatively high fraction of WCo-rich phase may increase the resistance to localized plastic deformation, while its potentially discontinuous distribution may reduce the likelihood of forming continuous brittle crack propagation paths. In contrast, the WCr-rich and σ phases in the NB joint may promote localized stress concentration because of deformation incompatibility with the surrounding γ matrix, facilitating crack initiation and propagation through the secondary phases or along their interfaces. Consequently, differences in the type, amount, and spatial distribution of secondary phases are likely important microstructural factors contributing to the distinct microhardness distributions, fracture locations, and high-temperature tensile properties of the CB and NB joints.

3.3. Microstructural Origin of the Differences in High-Temperature Tensile Strength

The high-temperature tensile properties of brazed joints are closely related to their microstructural characteristics, particularly the width of the brazed region, grain morphology, and the nature and distribution of secondary phases. Although both CB and NB joints exhibit polycrystalline microstructures within the brazed seams, their distinct solidification characteristics and phase distributions lead to considerable differences in deformation and fracture behavior. The CB joint is characterized by a relatively narrow polycrystalline region and finer grains, which may reduce the spatial extent of crystallographic orientation discontinuities and alleviate local deformation incompatibility during tensile loading. In contrast, the wider polycrystalline region in the NB joint contains more extensive grain boundaries and orientation discontinuities, potentially promoting localized stress concentration and facilitating crack initiation.

More importantly, the nature and distribution of secondary phases appear to play a critical role in governing the high-temperature mechanical response of the joints. In the CB joint, the WCo-rich phase, with an area fraction of approximately 3.1%, may contribute to local strengthening by impeding plastic deformation, while the surrounding γ matrix accommodates local strain and dissipates fracture energy. As a result, despite its relatively high microhardness of 610–690 HV0.2, the CB joint exhibits predominantly ductile fracture characteristics and achieves a tensile strength of approximately 630 MPa at 870 °C. In contrast, the NB joint contains WCr-rich and Cr-rich σ phases, with area fractions of approximately 1.6% and 0.9%, respectively. The deformation incompatibility between these

secondary phases and the surrounding γ matrix may induce localized stress concentrations, promoting crack initiation and subsequent propagation through the secondary phases or along their interfaces. This interpretation is consistent with the preferential fracture within the non-isothermal solidification zone and the predominantly cleavage-like fracture morphology observed in the NB joint, which exhibits a considerably lower tensile strength of approximately 470 MPa.

Notably, although the total area fraction of secondary phases in the CB joint (3.3%) is higher than that in the NB joint (2.5%), the CB joint exhibits superior high-temperature tensile performance. This finding suggests that the mechanical behavior of brazed joints is not simply determined by the amount of secondary phases but is also strongly influenced by their intrinsic properties, morphology, and spatial distribution. In the CB joint, the WCo-rich phase may enhance local deformation resistance without forming continuous preferential pathways for brittle crack propagation, thereby allowing the surrounding γ matrix to accommodate plastic deformation. Conversely, the WCr-rich and Cr-rich σ phases in the NB joint may act as preferential sites for crack initiation and propagation, leading to premature fracture under tensile loading. Therefore, the superior high-temperature tensile strength of the CB joint may be attributed to the combined effects of its narrower polycrystalline brazed region, finer grain structure, and more favorable secondary phase characteristics, which collectively improve local deformation compatibility and reduce the susceptibility to brittle fracture.

4. Conclusions

In this study, the effects of Ni-based (NB) and Co-based (CB) brazing filler alloys on the microstructure, secondary phase formation, and high-temperature tensile properties of DD5 single-crystal superalloy joints were systematically investigated. Particular attention was paid to the relationship between secondary phase characteristics and fracture behavior. The main conclusions are summarized as follows:

(1) Both Ni-based and Co-based filler alloys produced sound metallurgical joints in DD5 single-crystal superalloy without obvious pores or cracks. EBSD analysis revealed that polycrystalline microstructures formed within the brazed regions of both joints. The CB joint exhibited a finer grain structure, with an average grain size of approximately 56.3 μm, compared with 79.5 μm for the NB joint.

(2) The filler alloy composition significantly influenced the composition, morphology, and distribution of secondary phases within the brazed seams. The CB joint consisted primarily of a NiCo-rich γ matrix and skeletal WCo-rich and WCr-rich secondary phases, with area fractions of approximately 3.1% and 0.2%, respectively. In contrast, the NB joint contained WCr-rich and σ phases, with corresponding area fractions of approximately 1.6% and 0.9%, indicating distinct elemental partitioning and secondary phase formation characteristics between the two brazing systems.

(3) The CB joint exhibited a higher peak microhardness of approximately 690 HV0.2 compared with 610 HV0.2 for the NB joint, indicating greater local resistance to plastic deformation. This difference may be associated with the strengthening contribution of the WCo-rich phase in the CB joint. Furthermore, the interaction between the WCo-rich phase and the surrounding γ matrix may contribute to local deformation accommodation, whereas the WCr-rich and Cr-rich σ phases in the NB joint appear more susceptible to brittle cracking.

(4) The CB joint exhibited superior high-temperature tensile properties, achieving an average tensile strength of approximately 630 MPa at 870 °C, representing an improvement of 34% over the NB joint (470 MPa). Fractographic analysis revealed that the CB joint exhibited predominantly dimpled fracture features with localized quasi-cleavage characteristics, with fracture occurring mainly near the isothermal solidification

zone. In contrast, the NB joint displayed pronounced cleavage-like fracture features, with cracks preferentially initiating and propagating near the WCr-rich and Cr-rich σ phases within the non-isothermal solidification zone. The deformation incompatibility between these secondary phases and the surrounding γ matrix may promote localized stress concentrations and facilitate crack initiation and propagation, thereby reducing the high-temperature load-bearing capability of the NB joint.

(5) The favorable microstructural characteristics of the CB joint may enhance local deformation resistance while reducing susceptibility to premature brittle fracture, highlighting the potential of Co-based filler alloys for high-temperature brazing repair of DD5 single-crystal superalloy turbine blades.

Author Contributions: Conceptualization, D.Y. and X.Z.; Methodology, D.Y., T.H. and K.L.; Validation, G.L.; Formal analysis, X.Z.; Investigation, T.C., X.Z. and K.L.; Resources, S.L., T.C., G.L., B.H. and T.H.; Data curation, T.C., G.L. and B.H.; Writing—original draft, D.Y. and T.C.; Writing—review & editing, S.L., T.C., G.L., B.H. and T.H.; Supervision, S.L., T.H. and K.L.; Project administration, S.L. and K.L.; Funding acquisition, S.L. and T.H. All authors have read and agreed to the published version of the manuscript.

Funding: This study was supported by the Advanced Materials-National Science and Technology Major Project (2024ZD0600900).

Data Availability Statement: The original contributions presented in this study are included in the article. Further inquiries can be directed to the corresponding authors.

Conflicts of Interest: Authors Dongling Yang, Taili Chen, Tinghong Hou, Xuan Zhao, and Kuilin Luo were employed by the company Cheng Du Hang Li (Group) Industrial Co, Ltd. The remaining authors declare that the research was conducted in the absence of any commercial or financial relationships that could be construed as a potential conflict of interest.

References

1. Xia, W.; Zhao, X.; Yue, L.; Zhang, Z. A review of composition evolution in ni-based single crystal superalloys. *J. Mater. Sci. Technol.* **2020**, *44*, 76–95. https://doi.org/10.1016/j.jmst.2020.01.026.
2. Reed, R.C. *The Superalloys: Fundamentals and Applications*; Cambridge University Press: Cambridge, UK, 2008.
3. Wu, X.; Makineni, S.K.; Liebscher, C.H.; Dehm, G.; Rezaei Mianroodi, J.; Shanthraj, P.; Svendsen, B.; Bürger, D.; Eggeler, G.; Raabe, D.; et al. Unveiling the re effect in ni-based single crystal superalloys. *Nat. Commun.* **2020**, *11*, 389. https://doi.org/10.1038/s41467-019-14062-9.
4. Reed, R.C.; Tao, T.; Warnken, N. Alloys-by-design: Application to nickel-based single crystal superalloys. *Acta Mater.* **2009**, *57*, 5898–5913. https://doi.org/10.1016/j.actamat.2009.08.018.
5. Paik, S.; Dutta, B.K.; Kumar, N.N.; Tewari, R. Deformation and fracture initiation of Ni3Al intermetallic single crystal turbine blade. *Eng. Fract. Mech.* **2022**, *275*, 108812. https://doi.org/10.1016/j.engfracmech.2022.108812.
6. Zhao, Y.C.; Cheng, H.; Wang, H.; Zhao, Y.; Fan, Y.Z.; Wen, Z.X.; Yue, Z.F. Study on the method of avoiding resonance for double-walled single-crystal turbine blades based on crystallographic orientation design: A technique for solving macroscopic vibration problems from a microscopic scale. *Aerosp. Sci. Technol.* **2026**, *168*, 111013. https://doi.org/10.1016/j.ast.2025.111013.
7. Liu, J.; Li, Q.; Xie, Y.; Luo, J.; Zhang, C.; Wang, W.; Cao, K.; Liang, X.; Yang, L.; Zhou, Y. Microstructural evolution mechanism of aluminide coating on the inner hollow of superalloy blades during service in a real gas turbine. *J. Mater. Sci. Technol.* **2025**, *239*, 55–69. https://doi.org/10.1016/j.jmst.2025.02.076.
8. Chen, Y.; Yao, Z.; Dong, J.; Yang, H.; Ren, M.; Peng, J.; Leng, L.; Zhang, X.; Yang, J. Microstructural deterioration mechanism of directionally solidified ni-based superalloy used in first-stage industrial gas turbine blades after ultra long-term service. *Mater. Charact.* **2024**, *213*, 114000. https://doi.org/10.1016/j.matchar.2024.114000.
9. Guo, X.; Zheng, W.; Xiao, C.; Li, L.; Antonov, S.; Zheng, Y.; Feng, Q. Evaluation of microstructural degradation in a failed gas turbine blade due to overheating. *Eng. Fail. Anal.* **2019**, *103*, 308–318. https://doi.org/10.1016/j.engfailanal.2019.04.021.

10. Zhixin, Z.; Wu, Z.; Xiangde, B.; Xiaodong, Z. Failure analysis of a first stage turbine blade made of directionally solidified GTD111 superalloy and repaired by welding process. *Eng. Fail. Anal.* **2023**, *153*, 107570. https://doi.org/10.1016/j.engfailanal.2023.107570.
11. Wang, W.; Zhou, Y.; Jin, F.; Qin, Z.; Hong, X.; Wang, J.; Wang, B.; Lan, Q.; Li, P.; Dong, H. Co-doped amorphous filler metals enabled high-strength brazed DZ125 superalloys. *Mater. Charact.* **2026**, *240*, 116831. https://doi.org/10.1016/j.matchar.2026.116831.
12. Ren, X.; Li, W.; Xiong, H.; Ren, H.; Jing, Y.; Mao, W. Fast epitaxial brazing of DD6 single crystal superalloy using novel NiCoCrAlNbTi high entropy filler alloy. *J. Alloys Compd.* **2024**, *985*, 174082. https://doi.org/10.1016/j.jallcom.2024.174082.
13. Zhang, S.; Qu, W.; Teng, J.; Lyu, Y.; Zhao, H.; Zhuang, H. Development of the interlayer alloy using for TLP diffusion bonding of GH3230 superalloy based on the CALPHAD method. *Mater. Sci. Eng.* **2024**, *918*, 147434. https://doi.org/10.1016/j.msea.2024.147434.
14. Liu, J.D.; Jin, T.; Zhao, N.R.; Wang, Z.H.; Sun, X.F.; Guan, H.R.; Hu, Z.Q. Effect of transient liquid phase (TLP) bonding on the ductility of a ni-base single crystal superalloy in a stress rupture test. *Mater. Charact.* **2008**, *59*, 68–73. https://doi.org/10.1016/j.matchar.2006.10.018.
15. Li, S.; Wang, S.; Liu, P.; Mei, H.; Chen, Z.; Shao, T.; Bi, X.; Li, P.; Dong, H. Formation of multi-component M5B3 borides toward robust transient liquid phase bonded joints of DD5 single-crystal superalloy. *Mater. Charact.* **2026**, *237*, 116499. https://doi.org/10.1016/j.matchar.2026.116499.
16. Wang, G.; Sun, Y.; Wang, X.; Liu, J.; Liu, J.; Li, J.; Yu, J.; Zhou, Y.; Jin, T.; Sun, X.; et al. Microstructure evolution and mechanical behavior of ni-based single crystal superalloy joint brazed with mixed powder at elevated temperature. *J. Mater. Sci. Technol.* **2017**, *33*, 1219–1226. https://doi.org/10.1016/j.jmst.2017.01.027.
17. Cao, Y.; Hu, B.; Liu, Q.; Geng, L.; Du, B.; Hu, Y.; Zhang, H.; Pei, Y.; Li, S.; Gong, S. Study on microstructure evolution and failure behavior of Ni3Al-based single crystal superalloy joints brazed with ni-based filler. *J. Mater. Res. Technol.* **2024**, *30*, 7171–7186. https://doi.org/10.1016/j.jmrt.2024.05.104.
18. Li, W.; Jin, T.; Sun, X.F.; Guo, Y.; Guan, H.R.; Hu, Z.Q. Study of ni–cr–co–W–mo–B interlayer alloy and its bonding behaviour for a ni-base single crystal superalloy. *Scr. Mater.* **2003**, *48*, 1283–1288. https://doi.org/10.1016/S1359-6462(03)00045-9.
19. Li, S.; Li, J.; Shi, J.; Peng, Y.; Peng, X.; Sun, X.; Jin, F.; Xiong, J.; Zhang, F. Microstructure and mechanical properties of transient liquid phase bonding DD5 single-crystal superalloy to CrCoNi-based medium-entropy alloy. *J. Mater. Sci. Technol.* **2022**, *96*, 141–150. https://doi.org/10.1016/j.jmst.2021.04.024.
20. Pela, R.R.; Hsiao, C.L.; Hultman, L.; Birch, J.; Gueorguiev, G.K. Electronic and optical properties of core–shell InAlN nanorods: A comparative study via LDA, LDA-1/2, mBJ, HSE06, G0W0 and BSE methods. *Phys. Chem. Chem. Phys.* **2024**, *26*, 7504–7514.
21. Lang, Z.; Zou, T.; Ye, Z.; Wu, T.; Wang, W.; Yang, J.; Huang, J. High-performance brazing of single crystal superalloys with ni-cr-ta filler material. *Mater. Des.* **2024**, *237*, 112576. https://doi.org/10.1016/j.matdes.2023.112576.
22. Zhang, L.; Chen, J.; Yang, S.; Lu, H.; Qiu, C.; Zhang, Y.; Zheng, Y.; Qin, R. Review on high-energy beam repair of surface damages in ni-based single crystal superalloys. *Eng. Fail. Anal.* **2025**, *176*, 109612. https://doi.org/10.1016/j.engfailanal.2025.109612.
23. Xiang, H.; Tong, X.; Cai, X. Investigation of the microstructure evolution and mechanical properties of co-7Al-7W superalloy brazed joints using BNi-2 filler metal. *Mater. Charact.* **2026**, *234*, 116225. https://doi.org/10.1016/j.matchar.2026.116225.
24. Shi, J.; Liu, J.; Jin, F.; Tian, F.; Sun, X. Diffusion bonding of FGH98 superalloy and DD5 single crystal using pure Ni interlayer. *Mater. Today Commun.* **2023**, *37*, 107003. https://doi.org/10.1016/j.mtcomm.2023.107003.
25. Ren, X.; Bai, X.; Wang, H.; Zhai, Z.; Xiong, H.; Mao, W. In-situ borides precipitation and interface characterization of DZ125 superalloy joints brazed with high-entropy filler alloy. *Vacuum* **2026**, *244*, 114926. https://doi.org/10.1016/j.vacuum.2025.114926.
26. Song, J.; Lu, Z.; Peng, Y.; Gong, Z.; Zhao, C.; Xiong, J.; Li, J. Tensile behavior and failure mechanism of inconel 617 superalloy diffusion-bonded joints with Ni insert layer. *Mater. Sci. Eng.* **2026**, *973*, 150731. https://doi.org/10.1016/j.msea.2026.150731.
27. Zhao, S.; Shao, B.; Chen, H.; Hu, Y.; Pan, Z.; Liu, Y.; Wang, P.; Song, X.; Li, W. Wetting and interfacial behavior of high entropy alloy filler on rare earth silicate system: Phase analysis and first-principles calculations. *J. Mater. Sci. Technol.* **2025**, *233*, 223–238. https://doi.org/10.1016/j.jmst.2025.02.029.

Disclaimer/Publisher's Note: The statements, opinions and data contained in all publications are solely those of the individual author(s) and contributor(s) and not of MDPI and/or the editor(s). MDPI and/or the editor(s) disclaim responsibility for any injury to people or property resulting from any ideas, methods, instructions or products referred to in the content.